



# Synthesis of Metallo-conjugated Copolymer with Electron Deficient Main Chain and the Formation of Polymer–Carbon Nanotube Hybrids

King In Hau<sup>1</sup> · Kin Cheung Lo<sup>1</sup> · Wenjuan Xiong<sup>1</sup> · Lili Du<sup>1</sup> · Wai Kin Chan<sup>1</sup>

Received: 24 June 2019 / Accepted: 9 September 2019 / Published online: 30 September 2019  
© Springer Science+Business Media, LLC, part of Springer Nature 2019

## Abstract

We report the synthesis of a conjugated polymer incorporated with electron-deficient dipyrrophenazine units and pendant ruthenium complexes. The electronic transition and photophysical properties of the polymer were thoroughly studied. Due to the presence of an extended conjugated system, polymer main chain was able to interact strongly with carbon nanotube (CNT) surface by  $\pi$ – $\pi$  interaction, resulting in the formation of a dispersion in organic solvents. The polymer–nanotube hybrid was characterized by different microscopic and spectroscopic experiments. Raman spectroscopic results suggested that the electron density of the CNT decreased after the formation of polymer/nanotube hybrids, which suggests there is an electronic interaction between the polymer main chain and CNT.

**Keywords** Conjugated polymer · Carbon nanotube · Hybrid materials · Computation

## 1 Introduction

The functionalization of carbon nanotubes (CNTs) by polymeric materials has been a very interest research topic in the past decade because of the promising application potentials in a variety of areas such as sensing, optoelectronics, and biomedical applications [1–3]. In general, CNT can be functionalized by covalent or non-covalent approaches [4, 5]. In the first approach, the functional units are linked to the CNT surface via covalent bonds [6]. However, the  $\pi$ -conjugated system on CNT surface will be disrupted, resulting to changes in their electronic properties. The second approach relies on the non-covalent interaction (e.g.  $\pi$ – $\pi$  stacking) between the functional units and CNT surface [5], and is a preferable method because the  $\pi$ -electron system will not be affected as a result. In the past few years, our research group has been working on the synthesis of functional polymers for the formation of polymer–CNT hybrids and studying of their physical properties. Block copolymers and conjugated polymers functionalized with metal complexes have been synthesized [7, 8]. They were able to disperse both multiwalled and single walled CNTs (SWCNTs)

and form stable dispersions in organic solvents. It has been demonstrated that the presence of metal complexes on the polymer pendant group or main chain could strongly perturb the photophysical properties of the resulting hybrid materials. In one of the examples, it was shown that the ruthenium complex attached was able to enhance the photosensitivity of the polymer–CNT hybrid, which was confirmed by photoconductivity AFM experiments [9]. In other examples, the behavior of the transient species formed and the photoinduced electron transfer processes were found to be strongly affected by the introduction of metal complexes to the polymers [8, 10, 11]. Recently, it was found that the direction of photoinduced electron transfer in a polymer–CNT hybrid material is dependent on the relative energy level of the two entities [10]. CNT can function as either electron acceptor or donor after photoexcitation. This means that electron- or hole-carrying CNTs can be generated if a proper functional polymer is chosen. The resulting materials will have great application potentials in opto-electronic devices.

Based on the previous works, we have synthesized a metalloconjugated copolymer functionalized with electron deficient dipyrrophenazine units on the main chain and ruthenium terpyridine complexes at the pendant chain. It is envisaged that the electron deficient *N*-heterocyclic units and the sensitizing ruthenium complexes have significant effect to the physical properties to the hybrid formed. The polymer was able to disperse SWCNTs, and the interaction between

✉ Wai Kin Chan  
waichan@hku.hk

<sup>1</sup> Department of Chemistry, The University of Hong Kong, Pokfulam Road, Hong Kong, China

the polymer and CNTs was studied by various computation and spectroscopic techniques.

## 2 Experimental Sections

### 2.1 Reagents and Materials

2,7-Dibromofluorene, pyridine, tetra-*n*-butylammonium bromide, tetra-*n*-butylammonium hydroxide and ruthenium(III) chloride hydrate were purchased from Aldrich Chemical Co. 5,5'-Bis(4,4,5,5-tetramethyl-1,3,2-dioxaborolan-2-yl)-2,2'-bithiophene (**7**) was purchased from TCI Chemicals. 2,7-Dibromo-9,9-bis(6'-bromohexyl)fluorene (**1**) [12–15], 4'-(4-hydroxyphenyl)-2,2':6',2''-terpyridine (**2**) procedure [16], 5,6-diamino-1,10-phenanthroline [17, 18] (**4**), and 2,2':6',2''-terpyridine ruthenium trichloride (**9**) were synthesized according to literature procedures [19].

### 2.2 Instrumentations

<sup>1</sup>H and <sup>13</sup>C NMR spectra were recorded on Bruker DPX 300 NMR spectrometer (300 MHz and 75 MHz respectively) or Bruker Avance 400 NMR spectrometer (400 MHz and 100 MHz respectively). CDCl<sub>3</sub>, DMSO-*d*<sub>6</sub>, CD<sub>3</sub>CN-*d*<sub>3</sub> and DMF-*d*<sub>7</sub> were purchased from Cambridge Isotope Laboratories, Inc.; 1,1,2,2-tetrachloroethane-*d*<sub>2</sub> was purchased from Acros Organics. For <sup>1</sup>H NMR spectra, the signals were referenced to 0 ppm for tetramethylsilane internal standard in CDCl<sub>3</sub>; 2.50 ppm (residual proton of the solvent) for DMSO-*d*<sub>6</sub>; 2.05 ppm (residual proton of the solvent) for CD<sub>3</sub>CN-*d*<sub>3</sub>; 8.03 ppm (residual proton of the solvent) for DMF-*d*<sub>7</sub>; 6.00 ppm (residual proton of the solvent) for 1,1,2,2-tetrachloroethane-*d*<sub>2</sub>. In <sup>13</sup>C NMR spectrometry, the signals were referenced to the residual proton of the solvent at 77.16 ppm in CDCl<sub>3</sub>; 39.52 ppm (residual proton of the solvent) for DMSO-*d*<sub>6</sub>; 2.50 ppm (residual proton of the solvent) for CD<sub>3</sub>CN-*d*<sub>3</sub>; 163.15 ppm (residual proton of the solvent) for DMF-*d*<sub>7</sub>; 73.78 ppm (residual proton of the solvent) for 1,1,2,2-tetrachloroethane-*d*<sub>2</sub>. Positive-ion electron impact (EI) and fast-atom bombardment (FAB) mass spectra were collected from Finnigan MAT-95 mass spectrometer. UV–vis absorption spectra were collected from Varian Cary 50 UV–vis spectrophotometer. Micro-Raman spectroscopy was performed using Renishaw RM 3000 Micro-Raman system. He–Ne laser (633 nm) at 25 mW (with attenuator 10%) was used as excitation light source. The pristine SWCNTs and polymer/SWCNT hybrid samples were analyzed directly on PTFE membrane at the spectral range of 100 cm<sup>-1</sup> to 3200 cm<sup>-1</sup>. GPC was performed using a Waters GPC system equipped with a Styragel HR 3 column, a Waters 2414 refractive index detector and a Waters 2998 photodiode array detector. The GPC system was calibrated using polystyrene

standards. THF was used as the eluent with a flow rate of 0.4 ml min<sup>-1</sup>.

### 2.3 Monomer (3)

A mixture of 2,7-dibromo-9,9-bis(6'-bromohexyl)fluorene (**1**) (1.00 g, 1.54 mmol), 4'-(4-hydroxyphenyl)-2,2':6',2''-terpyridine **2** (1.0 g, 3.1 mmol), potassium carbonate (0.47 g, 3.4 mmol), potassium iodide (0.003 g, 0.018 mmol) and DMF (30 ml) were stirred under nitrogen at 100 °C for 16 h. After cooling to room temperature, the mixture was poured into 200 ml water and the product was precipitated. The mixture was filtered and product was recrystallized with ethanol and methanol mixture. White solid was obtained as the product. Yield 1.28 g (73%). <sup>1</sup>H NMR (400 MHz, CDCl<sub>3</sub>) δ (ppm): 8.73–8.71 (m, 4H), 8.69 (s, 4H), 8.66 (d, 4H, J = 7.9 Hz), 7.89–7.84 (m, 8H), 7.54–7.52 (m, 2H), 7.48–7.46 (m, 4H), 7.36–7.33 (m, 4H), 6.97 (dd, 4H, J = 8.7, 7.0 Hz), 3.91 (t, 4H, J = 6.5 Hz), 2.17–2.15 (m, 4H), 1.31–1.25 (m, 4H), 1.23–1.14 (m, 4H). <sup>13</sup>C NMR (75 MHz, CDCl<sub>3</sub>) δ (ppm): 156.5, 155.9, 149.2, 137.0, 130.4, 128.6, 126.3, 123.9, 121.5, 121.4, 118.4, 114.9, 68.1, 40.3, 29.7, 29.2, 25.8, 23.8. FAB-MS: *m/z* 1138.11 [*M*]<sup>+</sup>.

### 2.4 2,3-Bis(4-bromophenyl)pyrazino[2,3-*f*][1, 10]phenanthroline (6)

Monomer **6** was synthesized according to a modified procedure [20–22]. 1,10-Phenanthroline-5,6-diamine (**4**) (1.00 g, 4.76 mmol) and 4,4'-dibromobenzil (**5**) (1.93 g, 5.23 mmol) were added into a mixture of acetic acid (60 ml) and ethanol (60 ml). The reaction mixture was stirred under nitrogen atmosphere at 60 °C for 4 h. After cooling, the crude product mixture was filtered and washed with methanol and acetone. The residue was introduced to a 250-ml round-bottom flask and was stirred in acetone (200 ml) at room temperature for 12 h to dissolve the unreacted 4,4'-dibromobenzil. The product mixture was filtered and the residue was washed with acetone. White solid was collected as the product. Yield 2.15 g (84.0%). <sup>1</sup>H NMR (400 MHz, CDCl<sub>3</sub>) δ (ppm): 9.50 (d, 2H, J = 8.0 Hz), 9.29 (d, 2H, J = 3.0 Hz), 7.79 (dd, 2H, J = 8.1 Hz, 4.3 Hz), 7.56 (s, 8H). <sup>13</sup>C NMR (100 MHz, CDCl<sub>3</sub>) δ (ppm): 152.381, 152.338, 151.205, 147.764, 138.199, 137.345, 133.282, 133.231, 131.842, 131.592, 126.792, 124.050, 124.036. HREI-MS: *m/z* 541.9591 [*M*]<sup>+</sup>.

### 2.5 Polymer (8)

Polymer **8** was synthesized by the Suzuki coupling reaction [23–27]. Monomer **3** (0.420 g, 0.370 mmol), monomer **6** (0.200 g, 0.370 mmol), and **7** (0.308 g, 0.738 mmol) and were added to a 50-ml Schlenk tube under a nitrogen atmosphere. Anhydrous toluene (40 ml) and tetra-*n*-butylammonium

hydroxide (1 M solution in MeOH, 2.00 ml, 2.00 mmol) were added. The solution was further degassed by three freeze–pump–thaw cycles. Tetrakis(triphenylphosphine)palladium(0) (0.0214 g, 0.0185 mmol) was added to the reaction mixture. The reaction was carried out under nitrogen atmosphere at 60 °C for 48 h. After cooling, the mixture was filtered through a Celite bed to remove metal catalyst and insoluble polymer. The mixture was concentrated by rotary evaporation, and the polymer was obtained by precipitation in 200 ml methanol. The reprecipitation procedure was repeated twice and the residue was collected by filtration. Brown solid was obtained as product. Yield 0.182 g (29%).

## 2.6 Polymer (10)

The metalation procedure is based on literature procedures. Polymer **8** (0.100 g, 0.0592 mmol) and ruthenium complex **9** (0.052 g, 0.118 mmol) were added to a 50-ml Schlenk tube. The flask was degassed and filled with nitrogen gas thrice. Dry DMF (20 ml) was added and the reaction mixture was stirred at 100 °C under nitrogen for 48 h. After cooled to room temperature, the mixture was filtered to obtain the filtrate. Excess potassium hexafluorophosphate aqueous solution was added and the mixture was stirred for 15 min. The mixture was filtered and the residue was further washed with water, methanol, ethanol and diethyl ether. Brown solid was obtained as product. Yield 0.13 g (76%).

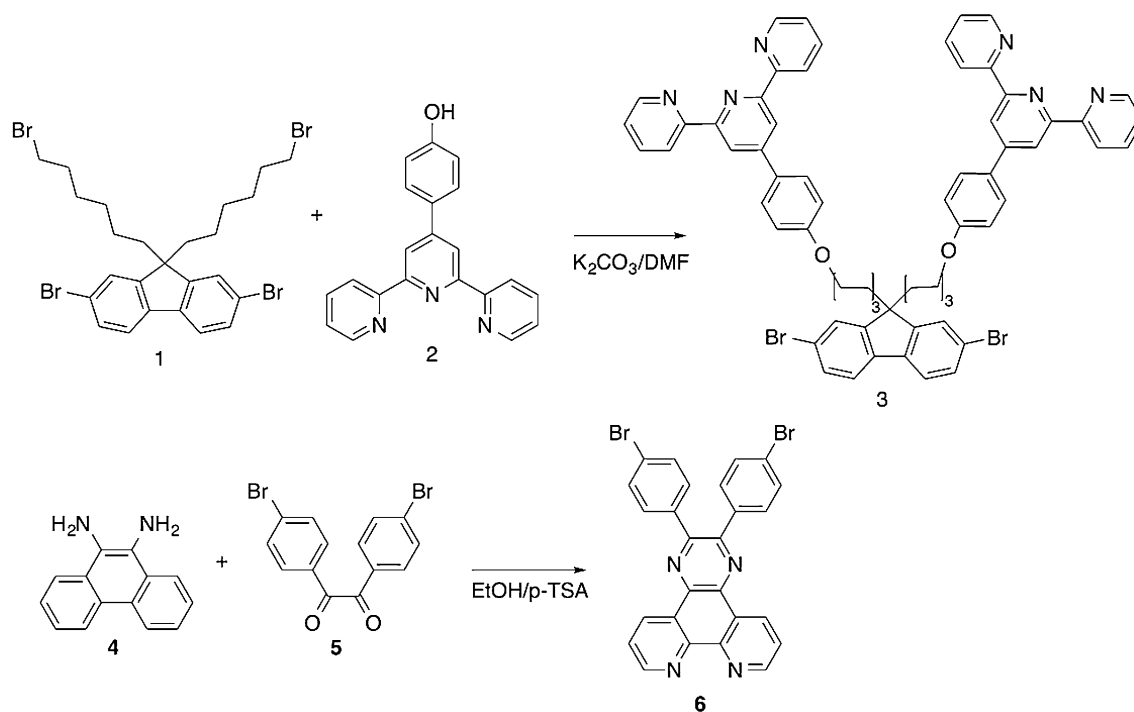
## 2.7 TDDFT Calculations

All the organic molecules involved in the DFT calculations were optimized at the Becke, three-parameter, Lee–Yang–Parr (B3LYP)/6-311G(d,p) level, while B3LYP/LANL2DZ was used in geometry optimization of ruthenium-containing molecules. Vibrational analysis was done in the same basis set to verify all the optimized structures were at the minimum of the energy surface. The spin-restricted singlet–singlet transitions were calculated by TDDFT calculations using B3LYP/6-311G(d,p) or CAM-B3LYP/6-311G(d,p) for those organic molecules, and B3LYP/LANL2DZ or CAM-B3LYP/LANL2DZ were used in the calculations of ruthenium-containing molecules. CPCM was used as the solvent model and chloroform was chosen to be the solvent ( $\epsilon=4.7113$ ). All calculations were performed in Gaussian 09 [28] in the GRIDPOINT and HPC2015 system of The University of Hong Kong. The spatial plots of molecular orbitals were generated by Gaussview 5.0 and Chem3D 15.1.

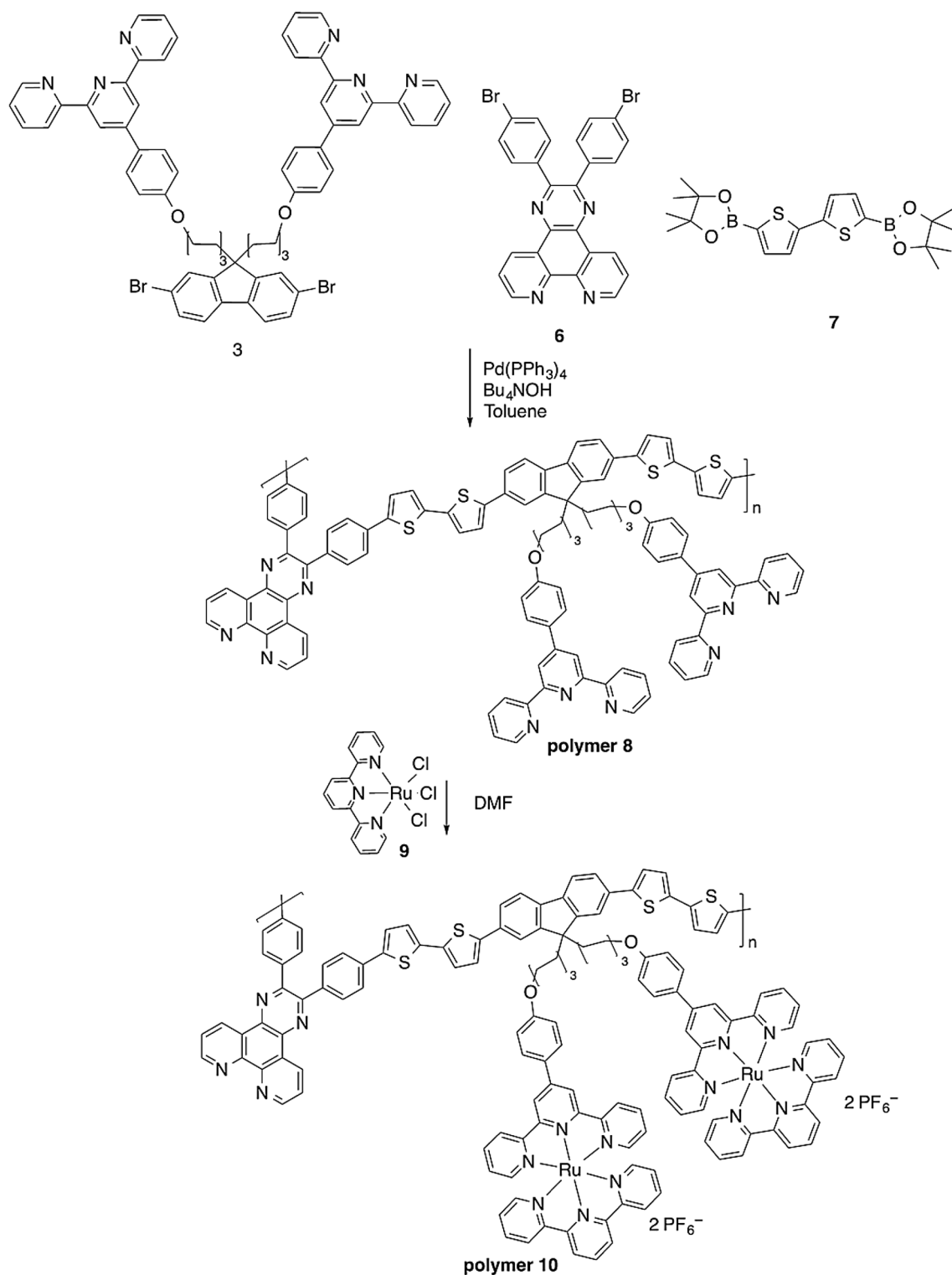
## 3 Results and Discussion

### 3.1 Synthesis and Characterization of Polymers

The synthesis of the monomers and polymers are shown in Schemes 1 and 2, respectively. Polymer **8** was synthesized



**Scheme 1** Synthesis of monomers

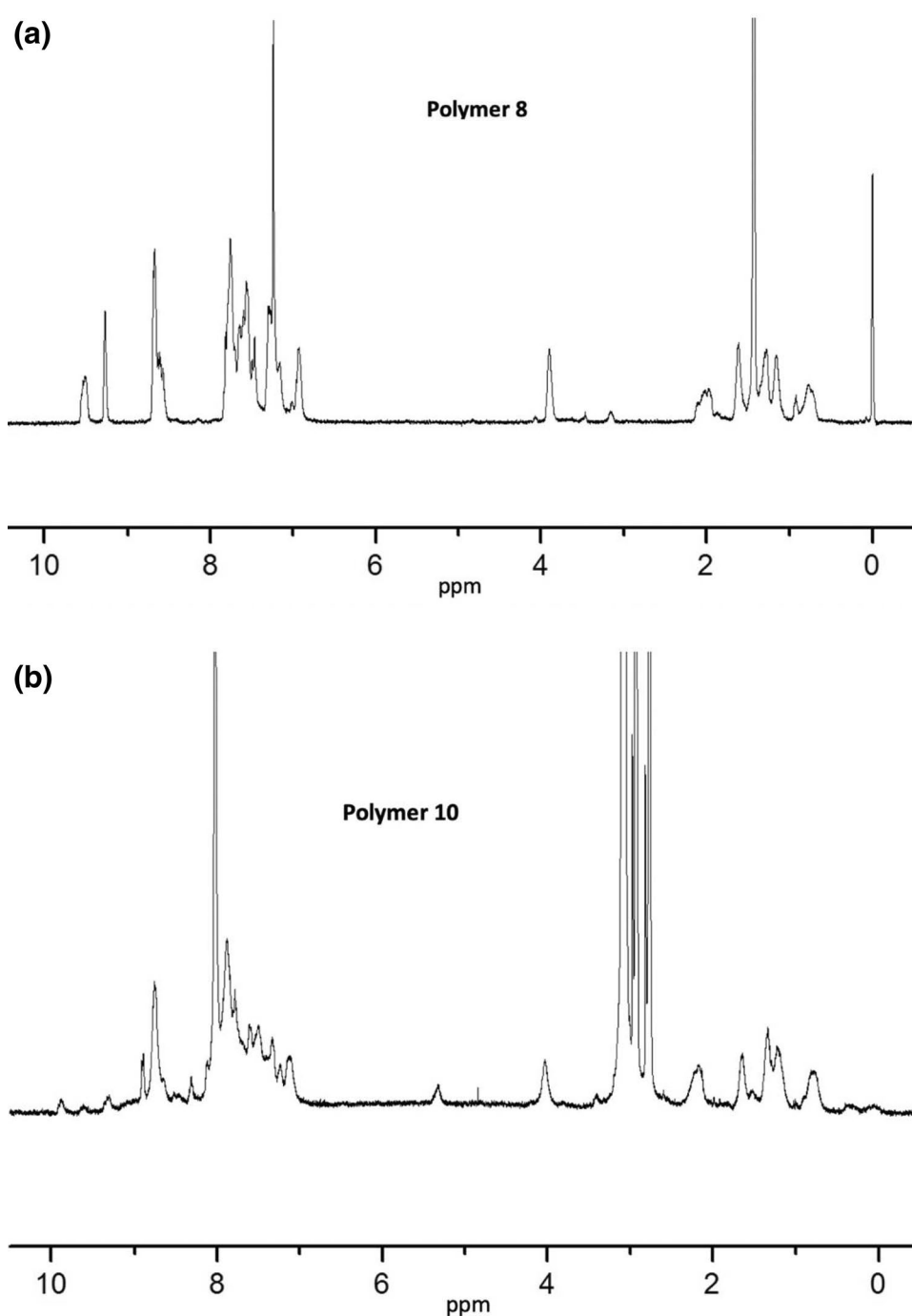


**Scheme 2** Synthesis of polymers **8** and **10**

by the Suzuki cross coupling reaction, and the ratio between monomer **3** and **6** was 1:1. The  $^1\text{H}$  NMR spectrum of polymer **8** is shown in Fig. 1a. The peak at  $\delta = 3.9$  ppm is assigned to the methylene protons at the fluorenyl unit, and

the peaks at 9.2–9.5 ppm are due to the protons at the phenanthroline ring. By comparing the integrals of these peaks, it can be calculated that the ratio of the phenanthroline and fluorenyl unit is 1:0.75. The change in monomer composition

**Fig. 1**  $^1\text{H}$  NMR spectra of **a** polymer **8** (in  $\text{CDCl}_3$ ) and **b** polymer **10** (in  $\text{DMF-}d_7$ )



compared to the feed ratio was probably due to the difference in the reactivity of monomer **3** and **6** in the coupling reaction. We attempted to measure the molecular weight of polymer **8** by GPC using THF as the eluent. However, the number average molecular weight obtained was in the range of 3000–4000. It should be noted that due to the presence of a “bending unit” in monomer **6**, the polymer chain formed does not favor a more extended chain conformation. This results in a relatively higher steric hindrance between adjacent monomeric units, lower reactivity for growing polymer

molecules. As a result, polymer with lower molecular weight was formed, and the more compact structure also results to a lower measured molecular weight. Polymer **8** was then subject to metalation by the reaction with ruthenium complex **9** in DMF. The metallopolymer **10** obtained is soluble in DMF due to the presence of the pendant charged Ru complexes, and its  $^1\text{H}$  NMR spectrum is shown in Fig. 1b. Compared to the  $^1\text{H}$  NMR spectrum of polymer **8**, addition peaks are observed at 9.7 and 9.9 ppm, which are assigned to the protons of the terpyridine ligand of the ruthenium

complexes [29, 30]. By comparing the integrals of the peaks at  $\delta = 9.2$  ppm in polymer **8** (corresponding to the protons on the middle pyridyl ring) and those at  $\delta = 9.6$  and  $9.9$  ppm in polymer **10** (corresponding to the protons next to the nitrogen atoms in the terpyridine ligands), the degree of metalation is estimated to be ca. 50%. We also attempted to measure the molecular weight of polymer **10** by GPC using NMP as the eluent. The  $M_n$  and polydispersity measured is 4500 and 1.8, respectively.

The normalized UV–vis absorption spectra of polymers **8** and **10** are shown in Fig. 2. Both polymers show two strong absorption peaks at ca. 285 and 390 nm. With reference to the electronic absorption properties of ruthenium terpyridine complexes [31], they are tentatively assigned to the intraligand  $\pi-\pi^*$  transition of the terpyridine unit and the  $\pi-\pi^*$  transition of the conjugated main chain, respectively. Polymer **10** also exhibits an additional broad absorption at ca. 500–550 nm, which is assigned to the metal-to-ligand charge transfer (MLCT,  $d-\pi^*$ ) transition at the ruthenium complex [30]. In order to study the main chain electronic absorption in more detail, TDDFT calculation has been performed in a model compound **8'**, of which the structure is shown in Fig. 3. The calculation was performed at the level of B3LYP/6-311G(d,p) and CAM/6-311G(d,p). The comparison between the absorption data for polymer **8** and computation results for **8'** are shown in Fig. 4. The CAM-B3LYP model gives a more accurate prediction to the electronic transitions than those of B3LYP. Therefore, only the electronic transitions calculated from CAM-B3LYP are used in subsequent discussion. The spatial plots of selected molecular orbitals of model compound **8'** are shown in Fig. 5, and some selected electronic transitions are summarized in Table 1. Since two absorption peaks at

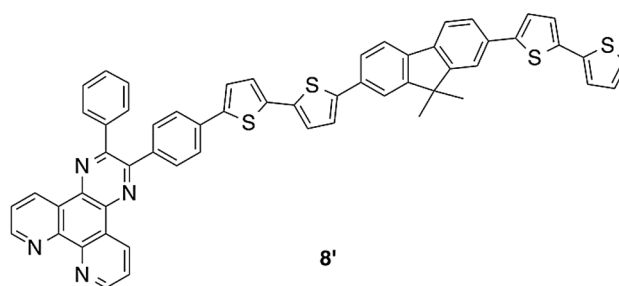


Fig. 3 Structure of the model molecule **8'** for the DFT calculation

285 and 390 nm are observed in polymer **8**, based on the TDDFT calculation results, the peak at 285 nm is assigned to the  $\text{HOMO} \rightarrow \text{LUMO} + 1$ ,  $\text{HOMO} - 1 \rightarrow \text{LUMO} + 2$ , and  $\text{HOMO} - 2 \rightarrow \text{LUMO}$  transitions. The peak at 390 nm is assigned to the  $\text{HOMO} \rightarrow \text{LUMO}$  transition at the main chain, and it can also be seen that the such absorption exhibits some charge transfer character. Therefore, the lower energy electronic transition has both  $\pi-\pi^*$  and intramolecular charge transfer character due to the presence of the electron rich bithiophene and the electron deficient phenanthroline units on the main chain.

### 3.2 Polymer–CNT Hybrids

Both polymers **8** and **10** were used in the dispersion of SWCNTs. In a typical dispersion process, a mixture of polymer and SWCNT was ultrasonicated in DMF, and a clear suspension was obtained after removal of other impurities by filtration and centrifugation. Figure 6 shows the morphologies of the functionalized SWCNTs obtained by TEM, and the image of a pristine SWCNT sample is also shown as a comparison. In general, the nanotube walls observed in pristine

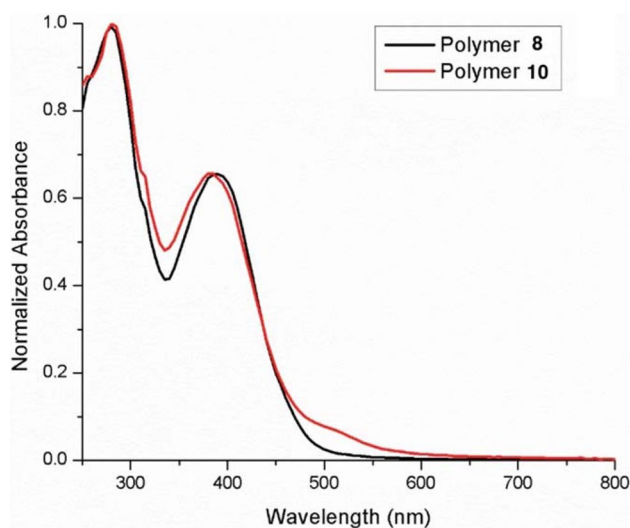


Fig. 2 Normalized UV–vis absorption spectra of polymers **8** and **10** in chloroform

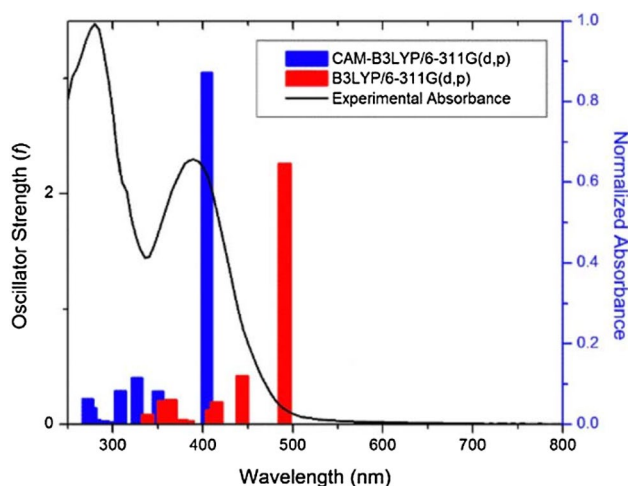
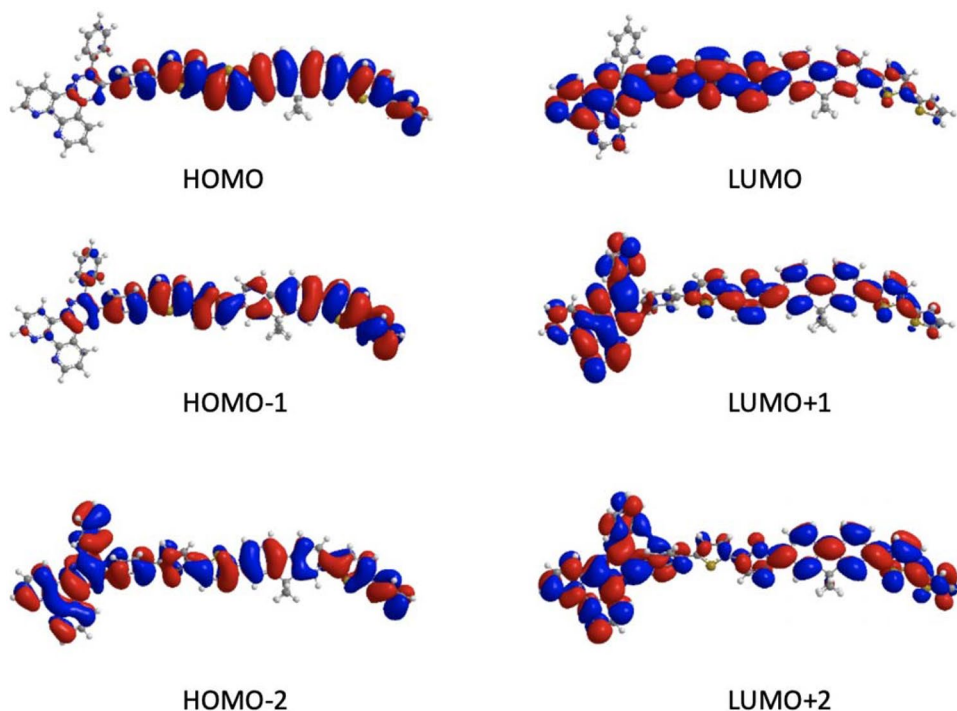


Fig. 4 Comparison of the UV–vis absorption spectrum and the computed electronic transitions obtained by different TDDFT models



**Fig. 5** Spatial plots of selected molecular orbitals of compound **8'** (isovalue = 0.02), calculated at CAM-B3LYP/6-311G(d,p) level of theory



**Table 1** Selected electronic excitations of model compound **8'** in chloroform with  $f > 0.2$ , calculated from TDDFT calculations at CAM-B3LYP/6-311G(d,p) level of theory

No.	$\lambda_{\text{calc}}$ (nm)	Vertical excitation energy (eV)	Oscillator strength $f$	Excitation	Configuration interaction (CI) expansion coefficient (% contribution)
1	490.8	2.526	2.262	H $\rightarrow$ L	0.655 (42)
2	443.5	2.795	0.418	H $\rightarrow$ L+1	0.649 (42)
3	364.0	3.405	0.207	H-1 $\rightarrow$ L+2	0.642 (41)
4	356.2	3.481	0.202	H-2 $\rightarrow$ L	0.625 (39)

H and L denote HOMO and LUMO respectively

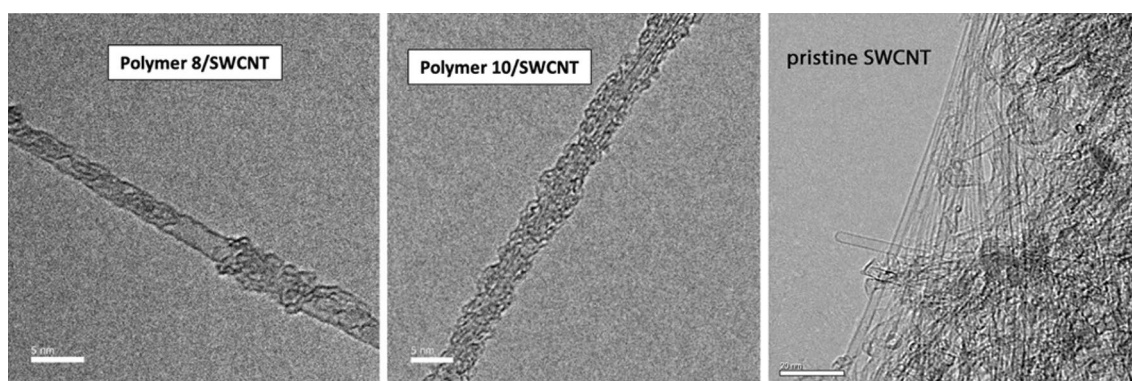


**Fig. 6** TEM images of polymer **8**/SWCNT, polymer **10**/SWCNT hybrid, and pristine SWCNT. The scale bar shown is 5 nm for the hybrids and 20 nm for the pristine sample

SWCNTs appear to be thin and solid dark lines with smooth surfaces, and the tubes also exist in clusters due to the strong interactions between individual tubes. For the polymer/

SWCNT hybrids obtained in our studies (Fig. 6), it can be seen that the tube surfaces are quite rough, possibly due to the attachment of a layer of polymer molecules. In addition,

more individual nanotubes can be found, which is the result of the dispersion process. To further confirm the presence of polymer molecules in the hybrids, EDX analyses were performed on both samples, and their EDX spectra are shown in Fig. 7. By comparing the spectra of polymer **8**/SWCNT and polymer **10**/SWCNT hybrids, additional peaks due to the presence of Ru can be seen in **10**/SWCNT. This indicates the presence of Ru complex in the sample, although a quantitative analysis cannot be performed. For polymer **8**/SWCNT hybrid, the dispersion formed was not very stable, which is probably due to the fact that DMF may not be a good solvent for the dispersion of SWCNT in a neutral polymer. Nevertheless, it was still possible to obtain the TEM image and perform EDX analysis, in which a strong signal due to the presence of sulfur was observed. For the hybrid formed between polymer **10** and SWCNT, the hybrid suspension

was stable for a prolonged period of time (more than 2 weeks) due to the presence of the charged ruthenium complexes at the side chain. EDX analysis showed the signals due to both sulfur and ruthenium. It can be seen that the presence of charged complexes has significant effect to the dispersibility of the polymer/SWCNT hybrid.

The UV–vis absorption spectra of the dispersions formed between polymers **8** and **10** with SWCNT are shown in Fig. 8. In general, the absorption band of polymer/SWCNT hybrids are broader than those of pure polymers, due to the overlapping of absorption with SWCNT. It can be seen that in Fig. 8a, the absorption maximum of polymer **8**/SWCNT hybrid shows a blue shift compared to the pure polymer. It is not clear what is the cause of such shift. It may be due to the relatively lower concentration and stability of the dispersion, and the broad absorption

**Fig. 7** EDX spectra of polymer **8**/SWCNT and polymer **10**/SWCNT

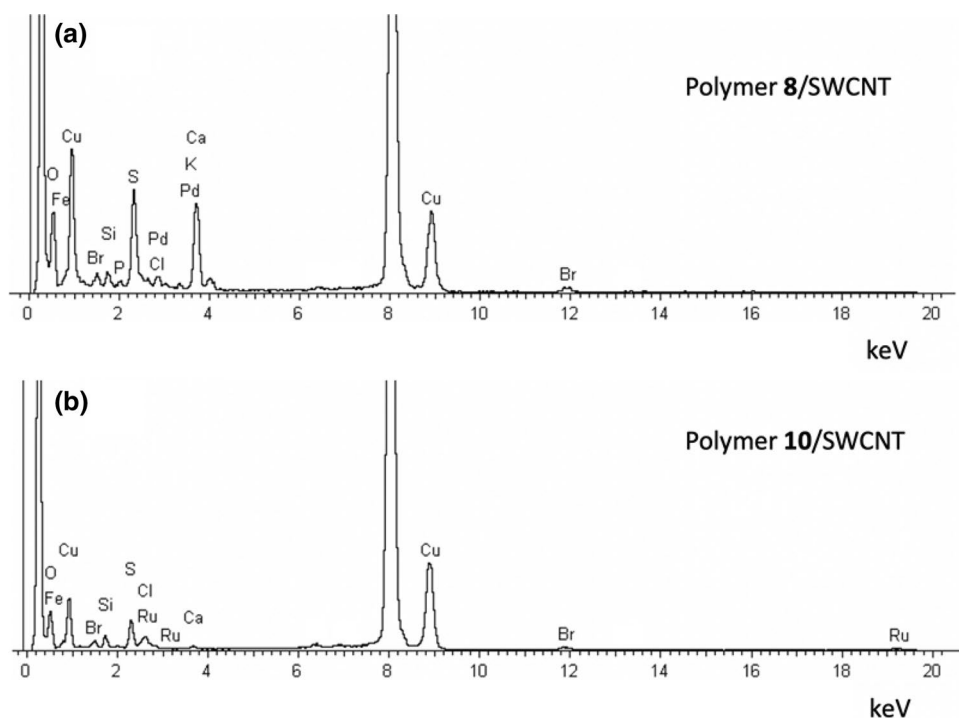
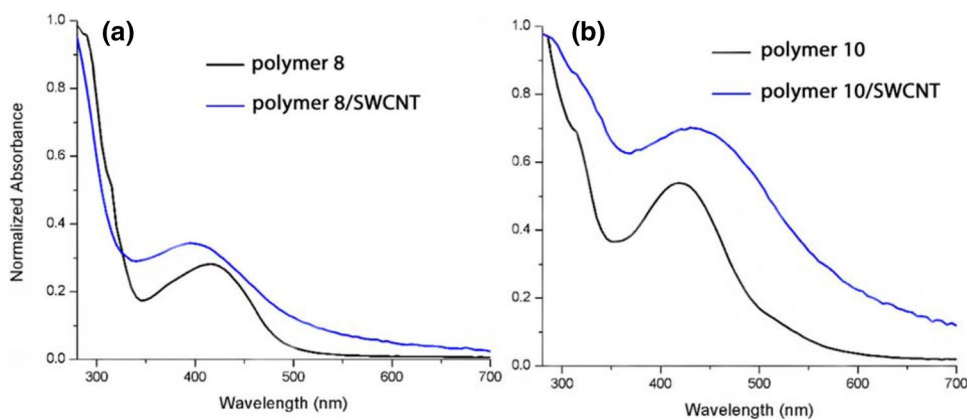


**Fig. 8** UV–vis absorption spectra of **a** polymer **8** and **b** polymer **10** and their SWCNT hybrid dispersions in DMF





of SWCNT dominates the absorption. On the other hand, there is a more remarkable change in the absorption spectra of polymer **10**/SWCNT hybrid compared to the pure polymer in DMF. The dispersion exhibits a broad absorption in the visible region due to SWCNTs, which also has a significant overlap with that of the ruthenium complexes.

The polymer–SWCNT hybrids were also subject to micro-Raman spectroscopy analysis, which can be used to scrutinize the vibrational modes of pristine and polymer/SWCNT hybrids. The Raman spectra of the pristine and polymer–SWCNT hybrids formed by polymers **8** and **10** are shown in Fig. 9, and some key spectroscopic data are summarized in Table 2. In general, the Raman spectra of SWCNTs consist of three main vibrational modes: (a) a series of low intensity peaks below 400  $\text{cm}^{-1}$  corresponding to the radial breathing mode (RBM), (b) a low intensity peak at ca. 1300  $\text{cm}^{-1}$  corresponding to the disorder induced mode (D-mode), and (c) a high intensity sharp peak at ca. 1590  $\text{cm}^{-1}$  corresponding to the tangential vibrational mode (G-mode) [32]. The frequency of peak due to the RBM can be used to estimate the diameter of the SWCNT by the equation [33]:

$$\omega_{RBM} = \frac{233.5 \text{ cm}^{-1}}{d} + 12.5 \text{ cm}^{-1},$$

where  $d$  is the diameter of SWCNT (in nm). By substituting the frequency of the RBM peaks observed in the equation, the diameters of the pristine and functionalized SWCNTs can be calculated (Table 2). The untreated SWCNTs have a wide distribution in diameter ranging from 0.6 to 1.6 nm. After functionalized with the polymers, the frequencies of the RBM bands suggest that polymers **8** and **10** favor the dispersion of SWCNT with larger diameter (from 1.0 to 1.6 nm).

**Table 2** Summary of micro-Raman spectroscopic data

Sample	Intensity ratio of D- to G-bands	Major RBM peaks observed ( $\text{cm}^{-1}$ ) and the calculated nanotube diameter (nm)
Pristine SWCNT	0.14	152 (1.60), 193 (1.24), 216 (1.10), 256 (0.92), 288 (0.82), 386 (0.60)
Polymer <b>8</b> /SWCNT	0.13	152 (1.60), 199 (1.24), 219 (1.10)
Polymer <b>10</b> /SWCNT	0.13	152 (1.60), 197 (1.24), 218 (1.10)

Chiral SWCNTs usually show a doublet peak in G-band, and exhibit fewer Raman active modes in the region of 400–1500  $\text{cm}^{-1}$ , while the intensity of the D-band can be regarded as a measure of defect intensity [33–35]. The G-bands observed in Fig. 9 consists of a single sharp peak, indicating the semiconducting nature of both pristine SWCNTs and SWCNTs in the polymer/SWCNT hybrids [32]. The intensity of D-band can be regarded as a measure of the defect intensity [32, 35]. An increase in D-band intensity indicates the presence of defect on the SWCNT surface (e.g. open tube ends or side-wall holes). Since the ratios between the D-band and G-band intensities are similar for the pristine SWCNT, polymer **8**/SWCNT and polymer **10**/SWCNT hybrids, indicating that there is no significant structural change or formation of defects after ultrasonication treatment. For the G- and RBM-bands, it has been reported that a frequency shift is the result of the change in SWCNT electron density [33, 34]. From Fig. 9, it can be seen that both the G- and RBM bands shift to the higher frequency after the functionalization with polymers **8** or **10** (from 1582  $\text{cm}^{-1}$  for pristine SWCNT to 1587  $\text{cm}^{-1}$  and 1586  $\text{cm}^{-1}$  for **8**/SWCNT and **10**/SWCNT hybrids, respectively). This

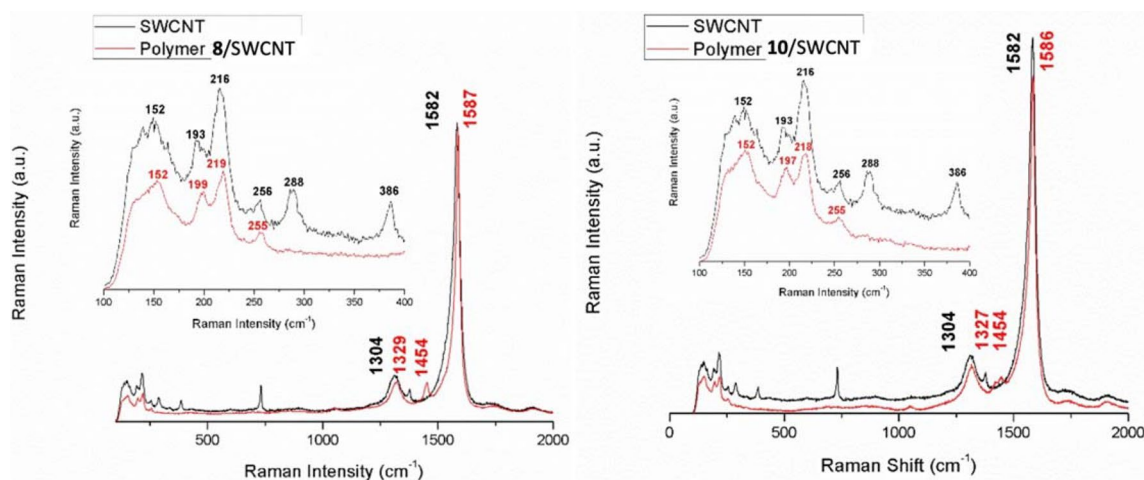


**Fig. 9** Raman spectra of pristine SWCNTs and the hybrids formed between polymers **8** and **10** with SWCNT

suggests a shift in electron density from the SWCNT to polymer (i.e. the SWCNTs became more electron-deficient after functionalization) [33, 34]. These results indicate there are notable interactions between the polymers and SWCNTs. Such phenomena were also observed in CNT functionalized with polythiophene based conjugated block copolymers [36]. It is envisaged that the shift in electron density is due to the presence of electron deficient dipyrroldiphenazine units on the main chain. Nevertheless, it is necessary to emphasize that at this stage, the nature of the electronic interactions is not fully understood. Further theoretical and experimental studies (e.g. ultrafast time-resolved spectroscopy) will be required in order to investigate the details of the excited states formation and the possible subsequent charge transfer processes.

## 4 Conclusions

A conjugated polymer incorporated with electron-deficient main chain and metal complex pendant chain were used in the dispersion of SWCNT. Due to the presence of ionic metal complex, a stable polymer–SWCNT dispersion was formed compared to the metal-free polymer. Raman spectroscopic results showed a shift in the G-band after the formation of the polymer/SWCNT hybrids. This suggests a shift in electron density from the nanotubes to the polymers and the presence of an electronic interaction between the species. In order to investigate the details of such interaction, more detailed photophysical spectroscopic studies, such as ultrafast time-resolved spectroscopic, will be required in order to understand how the polymer interact with the CNTs.

**Acknowledgements** This work was supported by the Research Grants Council of Hong Kong (HKU 700311P and HKU 700613P). The computation was conducted by using the HKU Information Technology Services Research Computing Facilities supported in part by the Hong Kong UGC Special Equipment Grants (SEG HKU09). NAMD was developed by the Theoretical and Computational Biophysics Group in the Beckman Institute for Advanced Science and Technology at the University of Illinois at Urbana-Champaign.

## References

1. A. Javey, J. Kong (eds.), *Carbon Nanotube Electronics* (Springer, New York, 2009)
2. M. Prato, K. Kostarelos, A. Bianco, *Acc. Chem. Res.* **41**, 60–68 (2008)
3. Y.P. Sun, K.F. Fu, Y. Lin, W.J. Huang, *Acc. Chem. Res.* **35**, 1096–1104 (2002)
4. D. Tasis, N. Tagmatarchis, A. Bianco, M. Prato, *Chem. Rev.* **106**, 1105–1136 (2006)
5. M.A. Herranz, N. Martin, in *Carbon Nanotubes and Related Structures*, ed. by D.M. Guldi, N. Martin (Wiley-VCH Verlag GmbH, Weinheim, 2010), pp. 103–134
6. X.H. Peng, S.S. Wong, *Adv. Mater.* **21**, 625–642 (2009)
7. C.H. Li, M.C.N. Alan, C.S.K. Mak, A.B. Djurisic, W.K. Chan, *ACS Appl. Mater. Interfaces* **4**, 74–80 (2012)
8. H.T. Shi, L.L. Du, W.J. Xiong, M.J. Dai, W.K. Chan, D.L. Phillips, *J. Mater. Chem. A* **5**, 18527–18534 (2017)
9. K.C. Lo, S.Y. Li, W.K. Chan, *J. Mater. Chem. C* **2**, 7739–7751 (2014)
10. W. Xiong, L. Du, K.C. Lo, H. Shi, T. Takaya, K. Iwata, W.K. Chan, D.L. Phillips, *J. Phys. Chem. Lett.* **9**, 3819–3824 (2018)
11. K.C. Lo, K.I. Hau, W.K. Chan, *Nanoscale* **10**, 6474–6486 (2018)
12. T.T. Do, H.S. Hong, Y.E. Ha, C.Y. Park, J.H. Kim, *Macromol. Res.* **23**, 177–182 (2015)
13. R.K. He, M. Hu, T. Xu, C.X. Li, C.L. Wu, X.Q. Guo, Y.B. Zhao, *J. Mater. Chem. C* **3**, 973–976 (2015)
14. S.J. Liu, K. Zhang, J.M. Lu, J. Zhang, H.L. Yip, F. Huang, Y. Cao, *J. Am. Chem. Soc.* **135**, 15326–15329 (2013)
15. D. Stay, M.C. Lonergan, *Macromolecules* **46**, 4361–4369 (2013)
16. K.C. Lo, PhD Thesis, The University of Hong Kong, 2014
17. J. Bolger, A. Gourdon, E. Ishow, J.-P. Launay, *Inorg. Chem.* **35**, 2937–2944 (1996)
18. A. Ghosh, A. Mandoli, D.K. Kumar, N.S. Yadav, T. Ghosh, B. Jha, J.A. Thomas, A. Das, *Dalton Trans.* **42**, 9312–9321 (2009)
19. J.P. Collin, S. Guillerez, J.P. Sauvage, F. Barigelli, L. Decola, L. Flamigni, V. Balzani, *Inorg. Chem.* **30**, 4230–4238 (1991)
20. R. Faust, S. Ott, *Dalton Trans.* (2002). <https://doi.org/10.1039/B110660K>
21. X. Li, S. Wu, D. Zhang, Z. Su, P. Lei, Z. Zhang, Z. Hu, W. Li, *Synth. Met.* **160**, 390–393 (2010)
22. L. Zhang, K.C. Lo, W.K. Chan, *Chem. Commun.* **50**, 4245–4247 (2014)
23. A.K. Dwivedi, G. Saikia, P.K. Iyer, *J. Mater. Chem.* **21**, 2502–2507 (2011)
24. R. Mallavia, F. Montilla, I. Pastor, P. Velasquez, B. Arredondo, A. Alvarez, C. Mateo, *Macromolecules* **38**, 3185–3192 (2005)
25. E. Puodziukynaite, L. Wang, K.S. Schanze, J.M. Papanikolas, J.R. Reynolds, *Polym. Chem.* **5**, 2363–2369 (2014)
26. D. Tuncel, M. Artar, S.B. Hanay, *J. Polym. Sci. A* **48**, 4894–4899 (2010)
27. R.M. Walczak, R.N. Brookins, A.M. Savage, E.M. van der Aa, J.R. Reynolds, *Macromolecules* **42**, 1445–1447 (2009)
28. M.J. Frisch, G.W. Trucks, H.B. Schlegel, G.E. Scuseria, M.A. Robb, J.R. Cheeseman, G. Scalmani, V. Barone, B. Mennucci, G.A. Petersson, H. Nakatsuji, M. Caricato, X. Li, H.P. Hratchian, A.F. Izmaylov, J. Bloino, G. Zheng, J.L. Sonnenberg, M. Hada, M. Ehara, K. Toyota, R. Fukuda, J. Hasegawa, M. Ishida, T. Nakajima, Y. Honda, O. Kitao, O. NAKAI, T. Vreven, J.A. Montgomery, J.E. Peralta, F. Ogliaro, M. Bearpark, J.J. Heyd, E. Brothers, K.N. Kudin, V.N. Staroverov, R. Kobayashi, J. Normand, K. Raghavachari, A. Rendell, J.C. Burant, S.S. Iyengar, J. Tomasi, M. Cossi, N. Rega, J.M. Millam, M. Klene, J.E. Knox, J.B. Cross, V. Bakken, C. Adamo, J. Jaramillo, R. Gomperts, R.E. Stratmann, O. Yazyev, A.J. Austin, R. Cammi, C. Pomelli, J.W. Ochterski, R.L. Martin, K. Morokuma, V.G. Zakrzewski, G.A. Voth, P. Salvador, J.J. Dannenberg, S. Dapprich, A.D. Daniels, O. Farkas, J.B. Foresman, J.V. Ortiz, J. Cioslowski, D.J. Fox, *Gaussian 09, Revision B.01* (Wallingford, 2009)
29. C.T. Wong, W.K. Chan, *Adv. Mater.* **11**, 455–459 (1999)
30. K.T. Potts, D.A. Usifer, A. Guadalupe, H.D. Abruna, *J. Am. Chem. Soc.* **109**, 3961–3967 (1987)
31. J.-P. Sauvage, J.-P. Collin, J.-C. Chambron, S. Guillerez, C. Coudret, V. Balzani, F. Barigelli, L. De Cola, L. Flamigni, *Chem. Rev.* **94**, 993–1019 (1994)
32. F. Hennrich, R. Krupke, S. Lebedkin, K. Arnold, R. Fischer, D.E. Resasco, M.M. Kappes, *J. Phys. Chem. B* **109**, 10567–10573 (2005)
33. S.M. Bachilo, M.S. Strano, C. Kittrell, R.H. Hauge, R.E. Smalley, R.B. Weisman, *Science* **298**, 2361–2366 (2002)

34. H. Gu, T.M. Swager, *Adv. Mater.* **20**, 4433–4437 (2008)
35. A.M. Rao, P.C. Eklund, S. Bandow, A. Thess, R.E. Smalley, *Nature* **388**, 257–259 (1997)
36. J.H. Zou, L.W. Liu, H. Chen, S.I. Khondaker, R.D. McCullough, Q. Huo, L. Zhai, *Adv. Mater.* **20**, 2055–2060 (2008)

**Publisher's Note** Springer Nature remains neutral with regard to jurisdictional claims in published maps and institutional affiliations.